Yu *et al. Journal of Ovarian Research* (2025) 18:299
https://doi.org/10.1186/s13048-025-01877-y

Journal of Ovarian Research

RESEARCH Open Access

Multi-omics reveals the immune and metabolic characteristics and associations in non-mucinous ovarian cancer

Hongkai Yu[1†], Chang You[2†], Ting Xu[3†], Ziyan Zhao[4], Danyang Wang[1], Lu Hu[2], Liangzhe Dai[5], Wanlin Zheng[6], Luyao Wang[1], Minghui Ji[3*], Tianchi Zhuang[3*] and Yingqi Yang[1*]

Abstract

Background The complex metabolic and immune characteristics of ovarian cancer and their interconnections can promote tumor immune evasion, ultimately leading to immunotherapy failure. A comprehensive understanding of these relationships can inform the development of diagnostic markers and more effective therapeutics.

Methods Mendelian randomization analysis identified the metabolic and immune characteristics of non-mucinous ovarian cancer. Glycosphingolipid metabolic gene signature was selected using Lasso and univariate Cox regression. Single-cell transcriptomics, proteomics, and spatial transcriptomics were applied to elucidate the expression of these genes and their association with immunological features, while cell-cell communication analysis explored potential molecular mechanisms. Prognostic models were constructed using multiple machine learning algorithms.

Results 13 metabolic and immune characteristics showed causally associations with non-mucinous ovarian cancer, including CD20 + B cells and the glycosphingolipid metabolism. PPIA-BSG mediated the cell-cell communication between CD20 + B cells and SUMF1 + malignant cells, promoting immune evasion driven by extracellular matrix remodeling. Prognostic models based on extracellular matrix genes co-experessed with SUMF1 demonstrated good predictive accuracy and generalizability across multiple independent datasets (maximum AUC = 0.732).

Conclusions In non-mucinous ovarian cancer, we identified two distinct cell subpopulations: CD20 + B cells and SUMF1 + malignant cells, which interact through the PPIA-BSG signaling axis. These findings may aid in identifying diagnostic markers and clinical therapeutic targets for this disease.

Keywords Non-mucinous ovarian cancer, Metabolism, Immunity, Multi-omics

[†]Hongkai Yu, Chang You and Ting Xu are contributed equally to this work.

*Correspondence:
Minghui Ji
jiminghui@njmu.edu.cn
Tianchi Zhuang
945998089@qq.com
Yingqi Yang
muyoung@stu.njmu.edu.cn

[1]The Second School of Clinical Medicine, Nanjing Medical University, Nanjing 211166, China
[2]School of Stomatology, Nanjing Medical University, Nanjing 211166, China
[3]School of Nursing, Nanjing Medical University, Nanjing 211166, China
[4]School of Rehabilitation Medicine, Nanjing Medical University, Nanjing 211166, China
[5]The First School of Clinical Medicine, Nanjing Medical University, Nanjing 211166, China
[6]School of Public Health, Nanjing Medical University, Nanjing 211166, China

Background

Ovarian cancer (OC) is the eighth most common cancer in women and the second leading cause of death from gynecologic cancers [1]. Its significant variations in immune and metabolic profiles further intensify the disease's heterogeneity. This complexity consequently undermines the effectiveness of immunotherapy [2, 3].

The tumor immune microenvironment (TIME) of OC is notably heterogeneity, characterized by genetic variations in tumor cells, diverse immune cell infiltration patterns, and varied immune responses. These all significantly influence tumor biological behavior and response to immunotherapy [4]. In high-grade serous ovarian carcinoma (HGSOC), HLA-E upregulation and impaired natural killer (NK) cell function frequently coincide with TP53 mutations [5, 6]. These alterations promote programmed death ligand 1 (PD-L1) overexpression and enhance glycolysis and glutamine catabolism via the mTOR pathway. Ovarian endometrioid carcinoma (OEC) is characterized by high tumor-infiltrating lymphocytes (TILs) infiltration due to microsatellite instability (MSI) or POLE mutations, while diminished B cell infiltration correlates with a poorer prognosis [7, 8]. Local immunosuppressive regulatory T cells (Tregs) activate the PPARγ pathway through lipid metabolites like prostaglandin E2 (PGE2), thereby promoting fatty acid oxidation (FAO) and cholesterol synthesis [9]. In clear cell ovarian carcinoma (CCOC), ARID1A loss and HIF-1α pathway activation cause defects in antigen presentation and abnormal angiogenesis. This low-immunogenicity microenvironment sustains hypoxia-adaptive metabolism through HIF-1α-dependent glycolysis and the pentose phosphate pathway (PPP) [10].

Furthermore, OC exhibits complex metabolic characteristics that influence the function of immune cells, promoting tumor immune evasion [11]. In serous ovarian carcinoma (SOC), the Warburg effect causes lactate accumulation in the tumor microenvironment (TME), directly suppressing anti-tumor immunity [12] and promoting Treg proliferation [13]. SOC cells utilize exogenous glutamine metabolism to release N-acetylaspartate (NAA), which induces macrophage polarization toward the M2 phenotype and upregulates PD-L1 expression [14–16]. In CCOC, hypoxia-induced abnormal glycogen accumulation and elevated reactive oxygen species (ROS) metabolism can impair immune responses by inhibiting T cell receptor signaling, while nicotinamide adenine dinucleotide phosphate (NADPH) generated via the PPP pathway strengthens antioxidant defenses to facilitate immune evasion [17]. OEC typically shares molecular features with endometrial cancer but may be metabolically more similar to CCOC [18]. Nevertheless, the metabolic characteristics of OC also provides potential therapeutic targets. For example, folate-targeted nanoparticles that inhibit glutamine metabolism have been shown to suppress tumor proliferation while enhancing antitumor immunity [19].

Here, a multi-omics analysis reveals the immune and metabolic characteristics of non-mucinous ovarian cancer and explores the relationship between metabolic changes and tumor immunity, thereby establishing a foundation for targeted therapies and biomarker exploration of non-mucinous ovarian cancer.

Methods

Data sources

The GWAS Catalog (accessions GCST90001391 to GCST90002121) provides genome-wide association study (GWAS) summary statistics for 731 immune cell traits, as reported by Zhao et al. in a study of 3,757 European individuals [20]. Summary statistics for 1,400 serum metabolites were obtained from the GWAS by Chen et al. (GCST90199621 to GCST902010209), which included data from 8,299 individuals covering 1,091 metabolites and 309 metabolite ratios [21]. Cathepsin GWAS data comprised two parts: data for 9 cathepsins from Li et al. (prot-a-718, prot-a-720, prot-a-722, prot-a-723, prot-a-725 to prot-a-729), derived from 3,301 individuals of European descent [22], supplemented with Cathepsin L1 data (GCST90012073) from 13 European cohorts totaling 21,758 participants, yielding 10 cathepsin datasets in total [23]. Inflammatory protein GWAS summary statistics for 91 traits (GCST90274758 to GCST90274848) were sourced from the study by Jing Hua Zhao et al. [24]. Summary statistics for 179 plasma lipids (GCST90277238 to GCST90277418) came from a GWAS by Ottensmann et al., which involved 7,147 Finnish individuals [25]. OC GWAS data encompassed non-mucinous epithelial ovarian carcinoma (NMEOC), HGSOC, low-grade serous epithelial ovarian carcinoma (LGSOC), endometrioid epithelial ovarian carcinoma (EEOC), CCOC, mucinous and mucinous cystic tumor, and SOC. OC GWAS data encompassed non-mucinous epithelial ovarian carcinoma (NMEOC), HGSOC, low-grade serous epithelial ovarian carcinoma (LGSOC), endometrioid epithelial ovarian carcinoma (EEOC), CCOC, mucinous and mucinous cystic tumor, and SOC. Histotype-specific epithelial ovarian carcinoma (EOC) data were obtained from a GWAS by Eileen O Dareng et al. (GCST90244167 to GCST90244171), including 23,394 cases of NMEOC, 15,588 cases of HGSOC, 2,729 cases of LGSOC, 2,877 cases of EEOC, and 1,427 cases of CCOC, totaling 25,981 EOC cases and 105,724 controls of European ancestry [26]. Mucinous and mucinous cystic tumor data originated from the FinnGen database (finngen_R11_C3_OVARY_MUCINO_EXALLC: 141 cases vs. 201,494 controls; finngen_R11_C3_OVARY_SEROUS_EXALLC: 1,016 cases vs. 201,494 controls) [27]. Further details on

all GWAS summary statistics are available in Supplementary Table S1.

We obtained RNAseq data and corresponding clinical information for 264 non-mucinous ovarian cancer patients from the The Cancer Genome Atlas (TCGA) database. Additional data were sourced from the Gene Expression Omnibus (GEO) under accession number GSE63885, which contains gene expression data from 101 ovarian cancer surgical samples, including 73 serous ovarian carcinoma, 12 endometrioid epithelial ovarian carcinoma, 9 clear cell ovarian carcinoma, and 7 undifferentiated types.

Single-cell transcriptome samples and associated clinical information for non-mucinous ovarian cancer were acquired from the GEO under accession numbers GSE115007, GSE118828, GSE130000, GSE147082, GSE151214, GSE154600, GSE154763, GSE158722, and GSE211956, as well as from the ArrayExpress database (E-MTAB-8107).

We obtained spatial RNA-seq matrices of primary tumor slices from 8 HGSOC patients from GEO [28], which were labeled OC1-OC8 (OC1: GSE211956-GSM6506110-SP1, OC2: GSE211956-GSM6506111-SP2, OC3: GSE211956-GSM6506112-SP3, OC4: GSE211956-GSM6506113-SP4, OC5: GSE211956-GSM6506114-SP5, OC6: GSE211956-GSM6506115-SP6, OC7: GSE211956-GSM6506116-SP7, OC8: GSE211956-GSM6506117-SP8).

69 glycosphingolipid metabolism genes and 568 extracellular matrix genes were obtained from the MsigDB database, specifically from the GOBP_GLYCOSPHINGOLIPID_METABOLIC_PROCESS, GO_EXTRACELLULAR_MATRIX gene sets.

Proteomics data is obtained from the Prospective ovarian JHU Proteome (PDC Study Identifier: PDC000110), with samples obtained from ovarian serous carcinoma.

Mendelian randomization (MR) analysis

In MR studies, single nucleotide polymorphisms (SNPs) serve as effective instrumental variables (IVs), and the eligible IVs are based on three assumptions: [1] Relevance assumption: The IVs are closely related to the exposure factor; [2] Independence assumption: The IVs should not be influenced by known or unknown confounding factors; [3] Exclusion assumption: The IVs affect the outcome factor only through the exposure factor. This study selected SNPs with a significance threshold of $P < 1e\text{-}05$. GWAS datasets for HGSOC, LGSOC, EEOC, mucinous and mucinous cystic tumor, SOC and CCOC were used as outcome datasets. The threshold for SNP linkage disequilibrium (LD) is $r^2 \leq 0.001$ and the genetic distance $\geq 10,000$ kb. An F statistic greater than 10 is used as a threshold to mitigate bias caused by weak IVs. Finally, Steiger filtering is applied to ensure causal direction. SNPs with inconsistent alleles or palindrome variants are excluded.

Protein expression analysis

We obtained 69 glycosphingolipid metabolism genes and used a non-parametric Wilcoxon rank-sum test to compare differences in protein expression levels of pathway genes. We obtained immunohistochemistry and immunofluorescence slides of non-mucinous ovarian cancer and normal tissues from the HPA database to validate differential gene expression levels. Sample and corresponding antibody information are provided in Supplementary Table S2, 3.

Survival analysis

We performed univariate Cox survival analysis using the survival package, fitting a Cox proportional hazards model with the coxph() function. Subsequently, a meta-analysis approach was employed to calculate the pooled hazard ratio (HR) and its 95% confidence interval (CI).

Gene set variation analysis

To investigate the function of MS4A1, we performed Gene Set Variation Analysis (GSVA). We utilized the z-score parameter algorithm from the GSVA package to assign scores to metabolic gene sets obtained from the Kyoto Encyclopedia of Genes and Genomes (KEGG) database. Differences in GSVA scores between the high and low MS4A1 expression groups were then analyzed with the Limma package.

Spearman correlation analysis

We employed Spearman correlation analysis to evaluate the relationship between immune checkpoints and glycosphingolipid metabolic gene signature selected by Lasso regression, with $P < 0.05$ considered statistically significant. This analysis used the GSE63885 dataset from the GEO database, which contains gene expression data from 101 °C surgical samples, including 73 SOC, 12 EEOC, 9 CCOC, and 7 undifferentiated types, representing the non-mucinous ovarian cancer category under investigation. ITPRIPL1, SIGLEC15, TIGIT, CD274, HAVCR2, PDCD1, CTLA4, LAG3, and PDCD1LG2 are key genes associated with immune regulation [29–33].

Immune microenvironment analysis

Tumor immune subtypes were classified according to the approach established by Thorsson V et al. [34], which assigned immune subtypes to each of more than 10,000 tumor samples representing 33 cancer types in TCGA. The Kruskal-Wallis rank sum test evaluated whether MS4A1 gene expression levels differed significantly across molecular subtypes in the OC dataset. Molecular subtype data originated from the UCSC Xena database.

Tumor samples were divided into groups based on the median value of gene expression. The easier package was used to quantify the levels of chemokines, tertiary lymphoid structures (TLS), IFN-γ, and inflammatory T cells in OC to evaluate corresponding immune features. Differences in the scores of different characteristics between the high- and low-expression groups were assessed with the Wilcoxon Rank Sum and Signed Rank Tests. According to the quartiles of gene expression, all patients were divided into four types: Q1, Q2, Q3, and Q4, where Q1 denotes the highest 25% and Q4 the lowest 25% of expression. In line with Thorsson V et al.'s framework for immune response and genomic status [34], average scores for each feature across the four patient groups were computed (excluding missing values) and visualized with the pheatmap package.

Immune infiltration data of OC was obtained from the public database TIMER2.0, and a comprehensive assessment of the content of different cell types and their Spearman correlation with gene expression was conducted using various algorithms (ABS, XCELL, TIMER, CIBERSORT, QUANTISEQ, MCPCOUNTER, EPIC), visualized with scatter plots and heatmaps. Differences in immune cell content between high- and low-expression groups, as estimated by the different algorithms, were compared using the non-parametric Wilcoxon rank-sum test and displayed in a heatmap.

The Tracking Tumor Immunophenotype (TIP) database systematically integrates ssGSEA and CIBERSORT to track, analyze, and visualize anti-tumor immune status and tumor-infiltrating immune cell proportions across seven stages of the cancer-immunity cycle. Spearman correlation analysis was employed to assess the correlation between target gene expression levels and TIP scores, as well as the self-correlation between TIP scores, and used the linkET package for visualization.

Single-cell transcriptome analysis

We processed and quality-controlled all single-cell sequencing matrices from the datasets EMTAB8107, GSE115007, GSE118828, GSE130000, GSE147082, GSE151214, GSE154600, GSE154763, and GSE158722 using the Seurat package. Cells selection was based on the following criteria: a Unique Molecular Identifier (UMI) count exceeding 1,000, between 500 and 4,000 expressed genes, and mitochondrial gene expression comprising less than 25% of the total UMI count. Cell type annotation was completed using the FindCluster function, with the resolution parameter set to 0.6 (resolution = 0.6) to balance between the number of clusters and the data structure. Expression levels of genes of interest across cell types were assessed using the Kruskal-Wallis rank-sum test.

Spatial transcriptomics analysis

Based on the single-cell transcriptomics quality control and clustering methods from the previous step, we performed deconvolution analysis preprocessing. Employing the get_enrichment_matrix and enrichment_analysis functions in the Cottrazm package, we generated an enrichment score matrix. The SpatialDimPlot function in the Seurat package visualized the predominant cell type within each spot, thereby achieving cell localization. Subsequently, we used the SpatialFeaturePlot function to visualize the gene expression landscape across spots for each samples. Finally, we performed Spearman correlation analysis to assess the correlation between the content of each cell in all spots and gene expression levels, with results visualized using the linkET package.

Cell-cell communication analysis

We used the CellChat package to analyze gene expression patterns that regulate intercellular communication, thereby providing a comprehensive view of signaling across different cellular environments. The intensity of intercellular communication was visualized using the netVisual_heatmap and netVisual_circl functions; The primary senders and receivers of intercellular communication and their connectivity were displayed using the netAnalysis_signalingRole_scatter and netVisual_aggregate functions, respectively; The netVisual_bubble function was used to demonstrate the ligand-receptor signaling pathways of intercellular communication.

Protein-protein interaction network

We constructed a protein-protein interaction network using the STRING database (string-db.org), imported the resulting network into Cytoscape (version 3.10.3), and scored each node with the cytoHubba plugin. The nodes were then ranked according to their Degree algorithm scores, and the top 50 genes were identified as key genes.

Weighted gene co-expression network analysis (WGCNA)

The top 5000 genes with the highest coefficient of variation (CV) was selected for analysis after low-quality samples and genes were excluded. A similarity matrix was constructed by calculating the Pearson correlation coefficient between genes, and a weighted adjacency matrix was generated using the soft-threshold power parameter β to confer scale-free properties on the network. The selection of the soft-threshold β is based on the scale-free topology model fitting index, with a fitting index > 0.85. The topological overlap measure (TOM) was then computed from the weighted adjacency matrix to evaluate the relative connectivity and neighborhood overlap among genes. Hierarchical clustering of genes was performed using the Dynamic Tree Cut method, a bottom-up algorithm, to identify co-expression modules. Modules with

a dissimilarity threshold of less than 0.25 were merged to reduce the number of modules and enhance their biological significance. Gene significance (GS) and module significance (MS) quantified the correlation of genes and modules, with stringent thresholds applied: |GS| >0.5 and |MM| >0.8.

Construction of prognostic models by various machine learning algorithms

Following previous research and optimizing the methodology [35, 36], we constructed prognostic models by using input genes directly as features and applied several machine learning algorithms: Lasso regression, Elastic Net, Ridge regression, Stepwise Cox regression, and CoxBoost. Lasso regression was implemented with the glmnet package, specifying the family parameter as cox, setting the alpha parameter to 1, and performing 10-fold cross-validation using the cv.glmnet function to select the optimal λ value. Both Elastic Net and Ridge regression were also implemented with the glmnet package, with the alpha parameter for Elastic Net tested across a range from 0.1 to 0.9 and set to 0 for Ridge regression. For Stepwise Cox regression, we first built a multifactor Cox regression model with the coxph function and then performed stepwise regression using the stepAIC function, evaluating all directions (both, forward, and backward). The CoxBoost model was developed by first optimizing the penalty parameter with optimCoxBoostPenalty, followed by cross-validation with cv.CoxBoost to finalize the model using the CoxBoost function. Model coefficients and their corresponding genes were extracted either with the coef function or from the model's regression coefficient slot.

Evaluation of the prognostic models

To evaluate the performance of the prognostic models, we employed the Receiver Operating Characteristic curve (ROC) and Area Under the Curve (AUC). The timeROC package calculated AUC values at 1, 3, and 5 years. These average AUC values were then visualized with the ComplexHeatmap package. Finally, a univariate Cox analysis was performed via the coxph function to calculate the HR values of the risk scores computed by the top-ranked algorithm across the datasets.

Statistics

The meta-analysis employed a random effects model to calculate a pooled hazard ratio (HR) with a 95% confidence interval (CI) from the included studies. Heterogeneity among the studies was assessed using a standard statistical test. All statistical analyses and visualizations were conducted with the Meta package in R (version 4.3.2). We used the glmnet package in R to perform Lasso regression for feature selection, setting family = cox to fit the Cox proportional hazards model. This model applies an L1 regularization constraint, automatically selecting variables significant for survival and shrinking the coefficients of insignificant variables to zero. The cv.glmnet function was used to perform 10-fold cross-validation. The optimal regularization parameter λ value was determined through cross-validation. When building the model, we set the maximum number of iterations to 1000 to ensure the convergence of the algorithm. Finally, use the coef function to extract the genes with non-zero coefficients and their regression coefficients at the optimal λ value. We used the VennDiagram package in R to draw Venn diagrams.

Results

CD20 + B cell and glycosphingolipid metabolism are key immune and metabolic characteristics of non-mucinous ovarian cancer

After excluding results that did not pass sensitivity analysis in MR analysis, we identified 13 immune and metabolic characteristics causally associated with more than three subtypes of non-mucinous ovarian cancer. Among them, CD20 on IgD + CD38 + B cell was negatively correlated with NMEOC (OR = 1.089, 95%CI: [1.046–1.134], P = 3.48e-05), HGSOC (OR = 1.080, 95%CI: [1.030–1.133], P = 0.002), and CCOC (OR = 1.164, 95%CI: [1.009–1.343], P = 0.037). Sphingomyelin (d18:1/19:0, d19:1/18:0) levels were positively correlated with NMEOC (OR = 1.110, 95%CI: [1.041–1.183], P = 0.002), HGSOC (OR = 1.097, 95%CI: [1.028–1.170], P = 0.005), and LGSOC (OR = 1.187, 95%CI: [1.008–1.398], P = 0.040). Hydroxypalmitoyl sphingomyelin (d18:1/16:0 (OH)) levels were positively correlated with NMEOC (OR = 1.074, 95%CI: [1.019–1.131], P = 0.008), EEOC (OR = 1.228, 95%CI: [1.077–1.400], P = 0.002), and CCOC (OR = 1.252, 95%CI: [1.043–1.504], P = 0.016). (Fig. 1a, see Supplementary Files for complete results of MR and sensitivity analysis). Both sphingomyelin and hydroxypalmitoyl sphingomyelin participate in glycosphingolipid (GSL) metabolism. Among the 69 GSL metabolism genes, the protein expression levels of GM2A, HEXA, HEXB, and SUMF1 were significantly increased in OC (Fig. 1b). We applied Lasso regression to remove collinearity in the gene set and obtained the GSL metabolic signature: B3GALNT1, GBA2, GM2A, HEXA, ITGB8, SCARB2, SUMF1, TM9SF2 (Fig. 1c, d). Intersection of this characteristic gene set with high-expression genes identified SUMF1 as a key GSL metabolism gene (Fig. 1e). The gene encoding CD20 is MS4A1. Univariate Cox regression analysis showed that MS4A1 was associated with progression-free survival (PFS) in OC (P = 0.020) and was a protective factor (HR = 0.92, 95%CI: [0.86–0.99]). A meta-analysis corroborated these findings (HR = 0.75, 95%CI: [0.60–0.94]), with low heterogeneity across survival periods

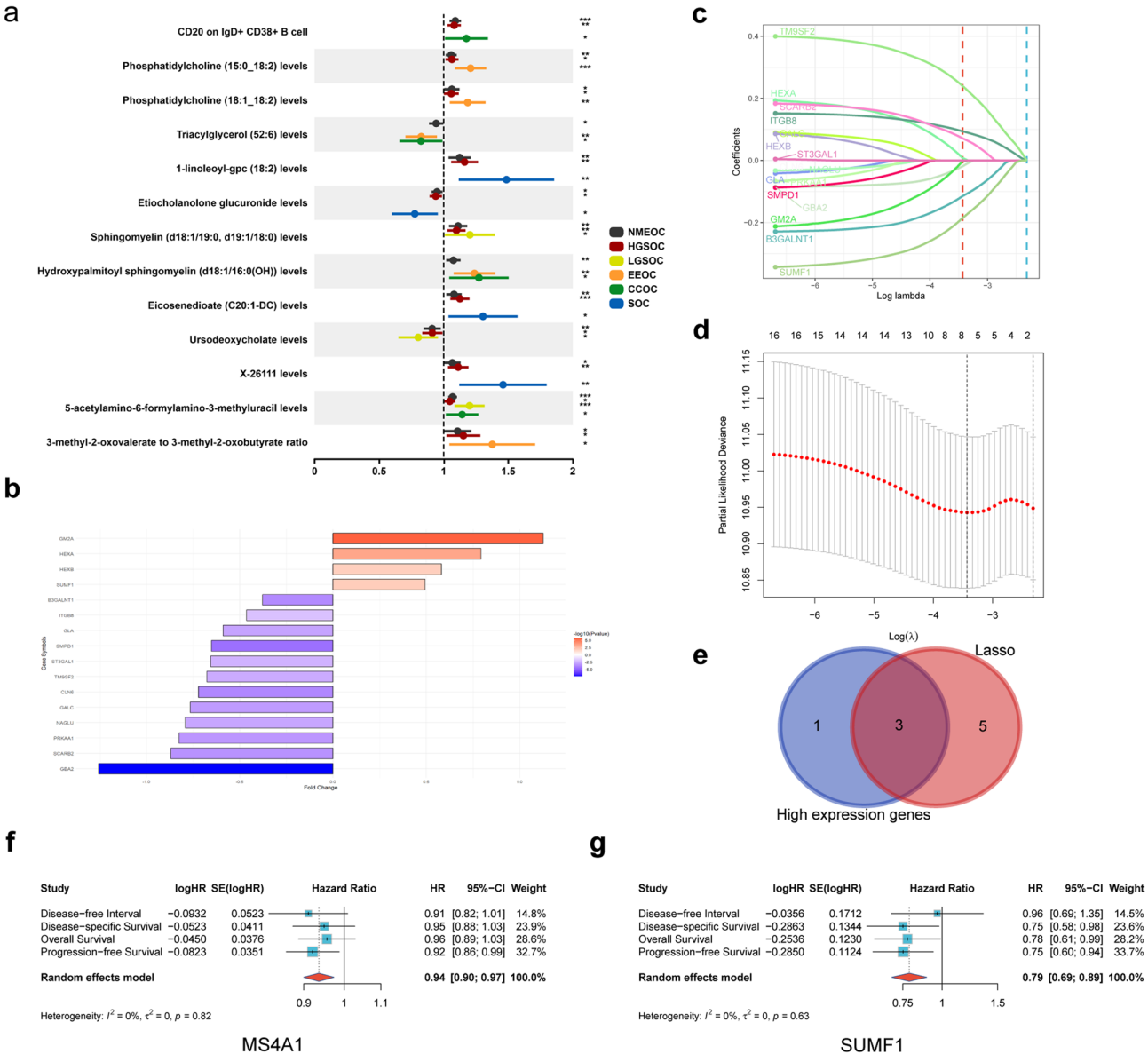

Fig. 1 Identification of the metabolic and immune characteristics of non-mucinous ovarian cancer. (**a**) The forest plot of the potential positive causal relationship between six non-mucinous ovarian cancer subtypes and immune and metabolic exposure factors; (**b**) Protein expression differential analysis of genes involved in GSL metabolism; (**c**) Lasso regression coefficient path plot. The horizontal axis represents the logarithm of the regularization parameter λ, and the vertical axis represents the magnitude of the regression coefficients; (**d**) Error analysis based on 10-fold cross-validation. The horizontal axis represents Log(λ), and the vertical axis represents the partial likelihood deviation; **e**) Venn Diagram illustrating the common factors shared by the feature gene set and the highly expressed gene set; (**f**) and (**g**) Forest plots of meta-analysis results for the univariate Cox survival analysis of MS4A1 and SUMF1, across four survival periods (DSS, OS, PFI, and DFI) in OC

($P = 0.82$) (Fig. 1f). SUMF1 was associated with disease-specific survival (DSS) (HR = 0.75, 95%CI: [0.58–0.98]), Overall survival (OS) (HR = 0.78, 95%CI: [0.61–0.99), and PFS (HR = 0.75, 95%CI: [0.60–0.94]) and was a protective factor. Meta-analysis confirmed these findings (HR = 0.79, 95%CI: [0.69–0.89]), with low heterogeneity across survival periods ($P = 0.63$) (Fig. 1g).

High expression of MS4A1 is associated with GSL metabolism and the activation of immune response in OC

The GSVA results revealed activation of specific metabolic pathways in the MS4A1 high-expression group, including glycosphingolipid biosynthesis in the ganglio, globo, and isoglobo series (Fig. 2a). Several GSL metabolic signature genes, including SUMF1, SCARB2, and GM2A, exhibited significant positive correlations with immune checkpoint genes such as PDCD1, HAVCR2, and LAG3 (Fig. 2b, c). Chemokine expression, IFN-γ

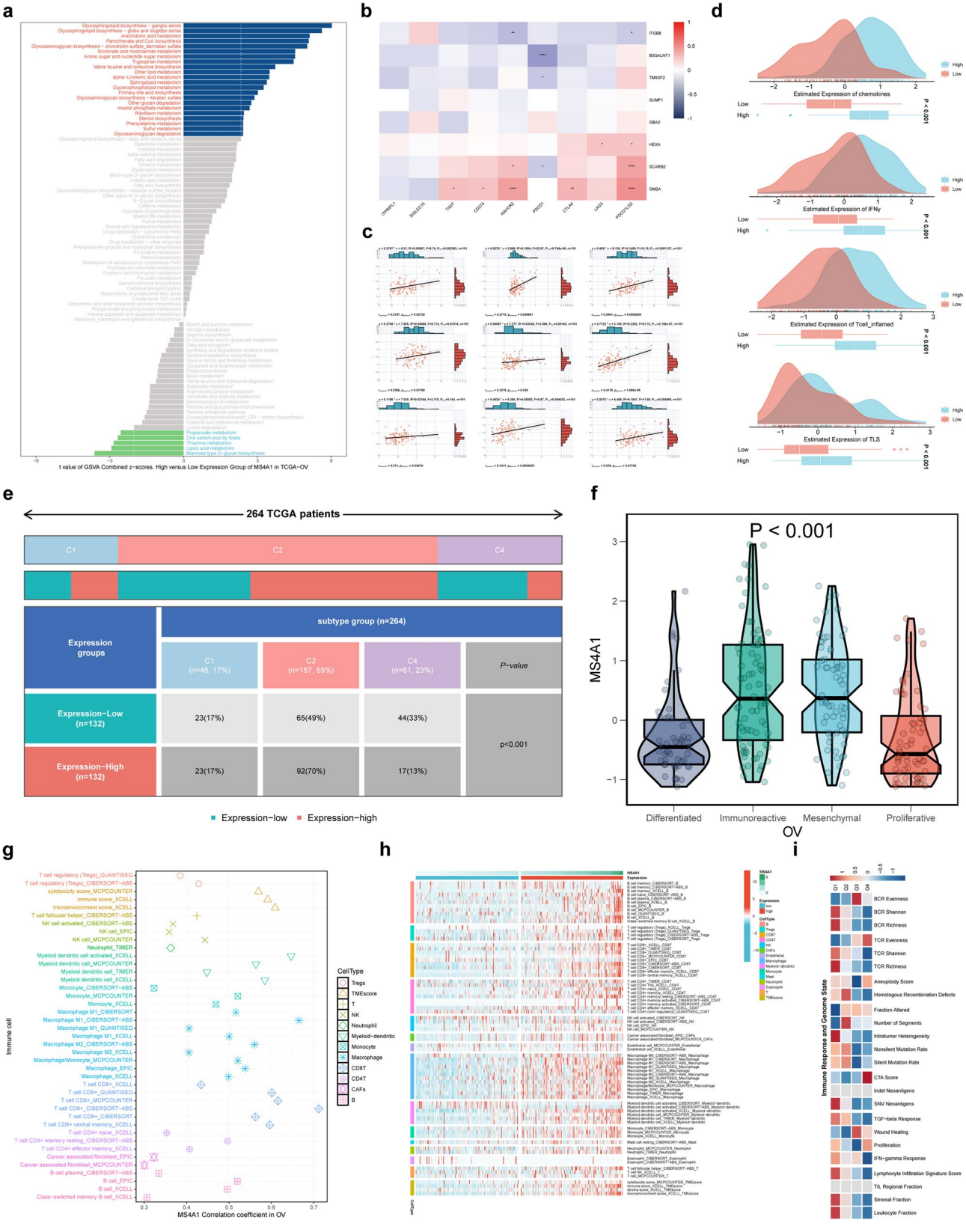

Fig. 2 (See legend on next page.)

(See figure on previous page.)

Fig. 2 Association between differential MS4A1 expression and metabolic pathways and the TIME. (**a)** Differences in GSVA scores for metabolic pathways between high and low MS4A1 gene expression groups. The horizontal axis represents the t-value of the GSVA score, while the y-axis represents different metabolic gene sets. Gray indicates no significant difference; (**b**) The heatmap illustrating the results of Spearman correlation analysis between key genes involved in GSL metabolism and immune checkpoints; (**c**) The scatter plots displaying the outcomes of Spearman correlation analysis for pairs exhibiting significant positive relationships. (**d)** The cloudrain plots displaying differences in the expression levels of chemokines, TLS, IFN-γ, and inflammatory T cells between the high and low MS4A1 expression groups; (**e**) Relationship between MS4A1 gene expression levels and different immune subtypes in 264 TCGA patients; (**f**) Violin plots illustrating the differential expression of MS4A1 in different molecular subtypes; (**g**) The lollipop plot demonstrating the correlation between MS4A1 gene expression and TIME evaluated using seven algorithms. Each cell type is identified by a specific color or pattern; (**h**) The heatmap revealing the differences in TIME between the high and low MS4A1 gene expression groups; **i**) Gene immune response scores and genomic instability scores within four phenotypes (Q1, Q2, Q3, Q4) based on quartile divisions of MS4A1 expression levels. Q1 corresponds to the top 25% of samples with the highest expression levels of MS4A1, whereas Q4 represents the bottom 25% with the lowest expression

levels, T-cell inflammation, and tertiary lymphoid structure (TLS) formation were also significantly upregulated in the MS4A1 high-expression group (all $P < 0.001$, Fig. 2d). The proportion of the C2 (IFN-γ dominant) subtype was significantly higher in the MS4A1 high-expression group than in the low-expression group, whereas the C4 (lymphocyte depletion) subtype was less frequent, and the C1 (tissue healing) subtype remained unchanged ($P < 0.001$, Fig. 2e). Among different molecular subtypes, MS4A1 expression was elevated in the Immunoreactive and Mesenchymal subtypes, but reduced in the Differentiated and Proliferative subtypes ($P < 0.001$, Fig. 2f). Immune infiltration analysis demonstrated positive correlations between MS4A1 and myeloid dendritic cells, M1 macrophages, CD8 + T cells, cytotoxicity score, immune score, and microenvironment score (Fig. 2g). In the MS4A1 high-expression group, the levels of immune cells—except for NK cells—and TME score were significantly elevated, while the levels of NK cells, cancer cells, and endothelial cells showed no significant difference compared to the MS4A1 low-expression group (Fig. 2h). We further explored the relationship between MS4A1 expression and immune infiltration as well as genomic status. These results indicated that MS4A1 overexpression corresponds to enhanced immune activity and altered genome state (Fig. 2i).

Expression patterns of MS4A1 and SUMF1 in non-mucinous ovarian cancer from the perspective of single-cell transcriptomics and spatial transcriptomics

Meticulous annotation identified the following cell types: CD8 + T cells, plasma cells, B cells, endothelial cells, monocytes, myofibroblasts, malignant cells, M1 macrophages, fibroblasts (Fig. 3a). The expression levels of MS4A1 and SUMF1 differed significantly across cell clusters (Fig. 3b); MS4A1 was primarily expressed in B cells, while SUMF1 exhibited high expression in malignant cells and fibroblasts (both $P < 0.001$, Fig. 3c). Though spatial transcriptomic analysis revealed no significant spatial localization for MS4A1, its expression was higher in low/mixed malignancy tissues and normal tissues. This suggested potential associations between MS4A1 and B cells and T cells in TME, as further demonstrated by Spearman correlation analysis. SUMF1 colocalized with tumor cells and showed its highest expression in (high) malignancy tissues. Spearman correlation analysis indicated that SUMF1 expression was significantly positively correlated with tumor cells. Notably, SUMF1 expression was negatively correlated with immune cells, including B/plasma cells, macrophages, and NK cells (Fig. 3d).

Cell-cell communication mediated by PPIA-BSG between SUMF1 + malignant cells and CD20 + B cells

Subsequently, cell-cell communication analysis was employed. Malignant cells, fibroblasts, and M1 macrophages acted as the principal signal senders, while B cells and M1 macrophages were the main receivers. The incoming interaction strength was greater for MS4A1 + B cells than for MS4A1 – B cells, and similarly stronger for SUMF1 + malignant cells than for SUMF1 – malignant cells (Fig. 4a). Among all signaling pathways identified by CellChat package, the macrophage migration inhibitory factor (MIF) pathway exhibited the highest communication intensity. Malignant cells, fibroblasts, M1 macrophages, epithelial cells, myofibroblasts, and plasma cells served as the primary senders of MIF signals, which were received mainly by M1 macrophages, monocytes, and MS4A1 + B cells (Fig. 4b). Analysis of ligand-receptor pairs indicated that, as receivers, MS4A1 + and MS4A1 – B cells did not differ significantly in their communication pathways with other cell types. As senders, MS4A1 + B cells interacted with malignant cells via the PPIA-BSG pathway, whereas this interaction was not observed between MS4A1 – B cells and malignant cells (Fig. 4c, d). Similarly, as senders, SUMF1 + and SUMF1 – malignant cells exhibited no significant differences in their communication pathways with other cells. As receivers, the key difference was that SUMF1 + cells primarily interacted with B cells, CD8 + T cells, and endothelial cells via the PPIA-BSG pathway, whereas whereas SUMF1 – malignant cells did not (Fig. 4e, f). These findings suggested that MS4A1 + B cells can communicate with SUMF1 + malignant cells via PPIA-BSG.

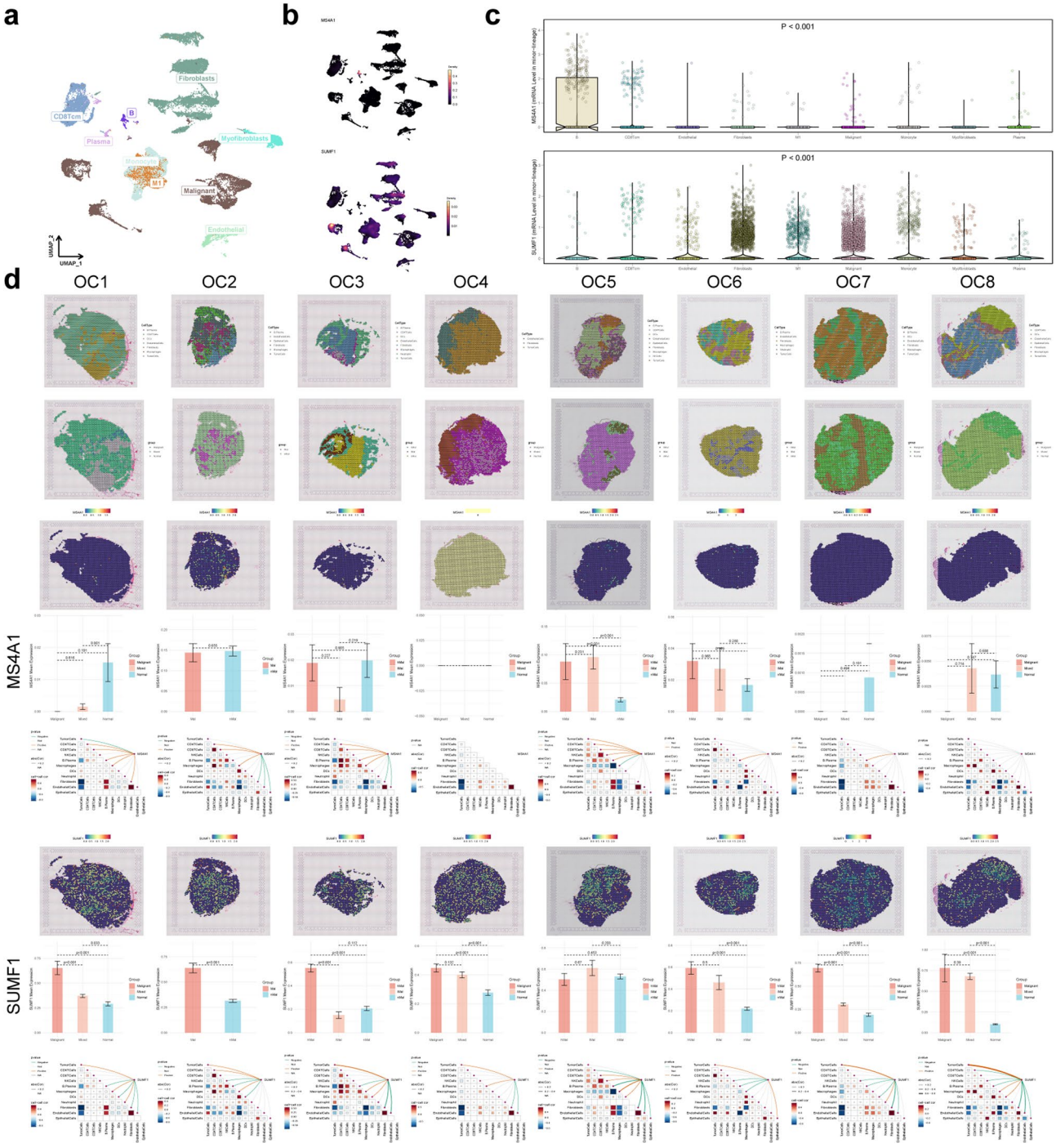

Fig. 3 Expression patterns of MS4A1 and SUMF1 at single-cell transcriptome and spatial transcriptome resolutions. (**a**) UMAP plot annotated with cell types; (**b**) Differential expression levels of MS4A1 and SUMF1 among different cell clusters; (**c**) Distribution and differential expression of MS4A1 and SUMF1 genes across different cell types; (**d**) Spatial transcriptomics analysis results from eight ovarian cancer samples. The labels of each tissue section are listed on the top of each column. The first row shows the localization of all cells after spatial transcriptome deconvolution. The second row displays the spatial localization of different malignant regions. The third and sixth rows depict the spatial transcriptome localization of MS4A1 and SUMF1 genes, respectively. The fourth and seventh rows exhibit the expression of MS4A1 and SUMF1 genes in high malignant/malignant, low/mixed malignant, and normal regions, respectively. The fifth and eighth rows present Spearman's correlation analysis between gene expression and TIME at the spatial transcriptome resolution for MS4A1 and SUMF1 genes, respectively

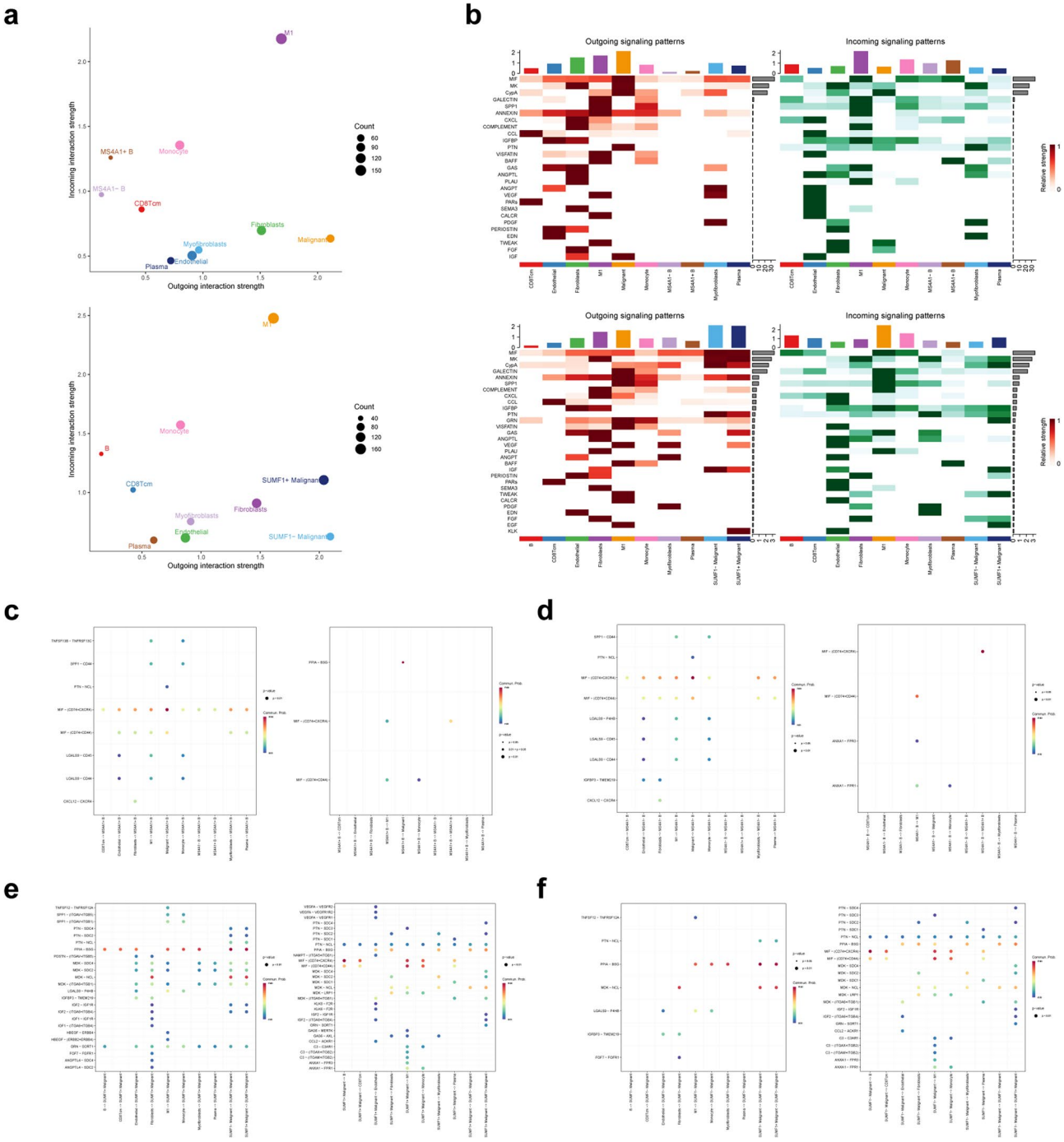

Fig. 4 Analysis of cell-cell communication between SUMF1 + malignant cells and CD20 + B cells. (**a**) Scatter plot illustrating the intensity of outgoing and incoming interactions in a two-dimensional manifold. The circle size indicates the number of significantly expressed ligand-receptor pathways in different cell populations; (**b**) Signal pathway strengths between different cell types. The vertical axis represents the cell sending or receiving the signal, while the horizontal axis denotes the pathway that receives or sends the signal. The pillars on the upper and right sides represent the accumulated strength of the vertical and horizontal axes, respectively; (**c**) MS4A1 + B cells, (**d**) MS4A1- B cells, (**e**) SUMF1 + malignant cells, and (**f**) Comparison of ligand-receptor pairs in cell-cell communication between SUMF1 + and SUMF1- malignant cells. Bubble color reflects communication probabilities, while bubble size represents computed *P*

Co-expressed extracellular matrix genes with SUMF1 are associated with OC prognosis

SUMF1 regulates diverse biological processes, including extracellular matrix (ECM) remodeling, through its role in sulfatase activation. To further investigate the biological functions of SUMF1, we performed WGCNA to identify gene modules strongly associated with SUMF1 in OC. The analysis revealed that samples in the highest 25% of SUMF1 expression (Q1) showed a significant positive correlation with the turquoise module (cor = 0.69, P < 1e-200), whereas those in the lowest 25% (Q4) were significantly negatively correlated (cor = −0.66, P < 1e-200) (Fig. 5a, b). By intersecting the ECM gene set with the turquoise module, 191 ECM genes co-expressed

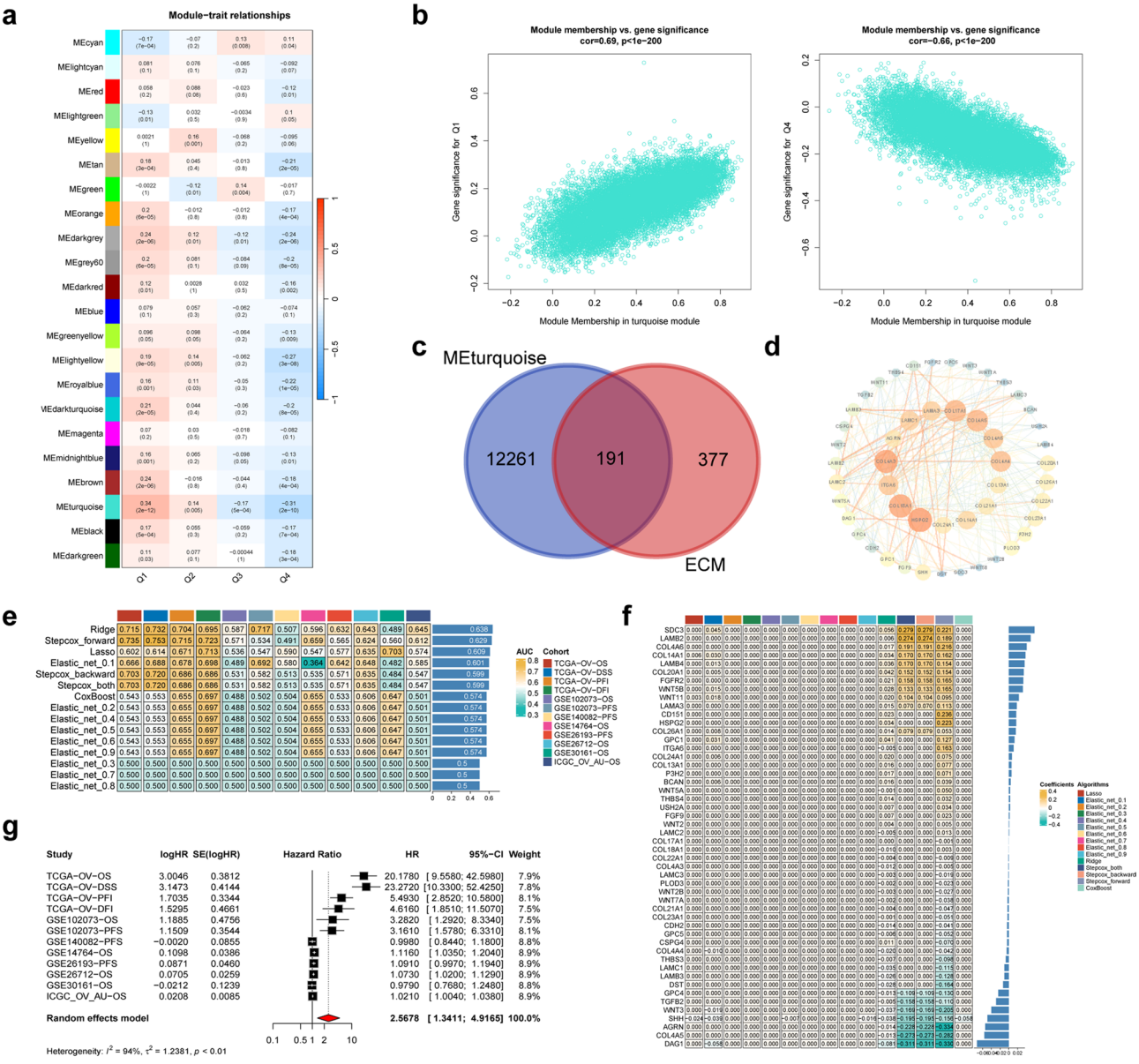

Fig. 5 Construction and evaluation of prognostic models based on ECM genes co-expressed with SUMF1 and multiple machine learning algorithms. (**a**) The heatmap illustrating the Pearson correlation between SUMF1 gene expression levels and various gene modules. Based on the quartile values of SUMF1 expression, four phenotypes are identified: Q1, Q2, Q3, and Q4. Q1 corresponds to the top 25% of samples with the highest expression levels of SUMF1, whereas Q4 represents the bottom 25% with the lowest expression; (**b**) Scatter plot demonstrating the correlation between Module Membership and Gene Significance; (**c**) Venn diagram displaying the overlapping genes between the ECM gene set and the turquoise module gene set; (**d**) The top 50 hub genes identified through Protein-Protein Interaction analysis using Cytoscape; (**e**) Comparison of the average AUC values at 1, 3, and 5 years for prognostic models constructed by various algorithms. The heatmap showcases the average AUC values for prognostic models constructed by various algorithms at 1, 3, and 5 years. The algorithms are ranked from top to bottom based on their average AUC values, from highest to lowest; (**f**) Coefficients of each gene in different prognostic models; (**g**) Meta-analysis of survival hazard ratios for prognostic models

with SUMF1 were obtained (Fig. 5c). From these, the top 50 hub genes were selected using Cytoscape (Fig. 5d) for prognostic model construction. Prognostic models were constructed with various machine learning algorithms, and a comprehensive evaluation was performed by comparing the average AUC values at 1 year, 3 years, and 5 years. Ultimately, the Ridge model achieved the highest predictive performance (maximum AUC = 0.732) (Fig. 5e). Genes including SDC3, LAMB2, COL4A6, LAMB4, COL20A1, FGFR2, and WNT58 contributed substantially across multiple models. As shown in Fig. 5g, the prognostic model exhibited consistent performance across different survival periods in multiple datasets, indicating robust predictive accuracy and generalization ability.

High expression of BSG in non-mucinous ovarian cancer and its association with immunosuppression

We analyzed BSG expression in non-mucinous ovarian cancer across multiple resolutions. Immunohistochemistry revealed BSG upregulation in tumor tissues (Fig. 6a), while immunofluorescence localized the protein primarily to vesicles and membranes at the subcellular level (Fig. 6b, Supplementary Table S2, 3). Single-cell transcriptomics analysis indicated that BSG expression was highest in malignant cells and fibroblasts ($P < 0.001$, Fig. 6c, d). BSG negatively correlated with cancer immune cycle scoring (Fig. 6e). Under various computational algorithms, immune cell infiltration was significantly reduced in the BSG high-expression group relative to the low-expression group (Fig. 6f). Inflammatory T cell expression was also markedly lower in the BSG high-expression group ($P = 0.008$, Fig. 6g). Finally, spatial transcriptomics analysis further demonstrated that BSG colocalized with malignant cells and fibroblasts. Interestingly, BSG expression was elevated at the interface between malignant and normal tissue. Across multiple OC samples, BSG was was more highly expressed in regions of low/mixed malignancy regions (Fig. 6h). These findings imply a potential role for BSG in ECM formation or function in non-mucinous ovarian cancer.

Discussion

The metabolic state and immune infiltration in TME significantly influence antitumor immune responses. This study is the first to confirm a causal relationship between non-mucinous ovarian cancer and CD20 + B cells, which is a protective factor for prognosis. CD20 is highly expressed on B cells at low differentiation stages and serves as a marker for naïve, germinal center, and memory B cells [37]. Elevated CD20 + B cell infiltration indicates active B cell proliferation in TME, which may explain the improved prognosis observed in non-mucinous ovarian cancer with high infiltration. Previous studies have also identified CD20 + B cells as significant prognostic factors in HGSOC [38]. A separate large cohort study further reported that infiltrating CD20 + B cells exert an independent favorable prognostic effect in primary tumors of colorectal cancer [39].

The immune subtyping of non-mucinous ovarian cancer in this study was based on the framework established by Thorsson V et al. in *The Immune Landscape of Cancer* [40], which has since been extensively validated by the TCGA consortium and numerous independent investigations [41–44]. Thorsson V et al. delineated these subtypes using a range of immunological features, including macrophage and lymphocyte signatures, the Th1:Th2 cell ratio, intratumoral heterogeneity, aneuploidy, neoantigen load, overall cellularity, immunomodulatory gene expression, and prognostic correlates. Nevertheless, because the specific gene sets applied for subtyping were not disclosed by Thorsson V et al., validating this classification in external datasets remains unfeasible at present.

Although external validation of the immune subtyping could not be conducted, our characterization of the TIME aligned closely with these subtypes. Notably, 70% of samples in the MS4A1 high-expression group were classified as the C2 immune subtype, a proportion significantly greater than that in the low-expression group ($P < 0.001$). The C2 subtype is distinguished by a predominant IFN-γ signature, heightened M1/M2 macrophage polarization, and a robust CD8 + T cell signal [45]. In the present study, IFN-γ expression was markedly upregulated in the MS4A1 high-expression group ($P < 0.001$). Immune infiltration analysis employing seven computational algorithms revealed a positive correlation between MS4A1 expression and the abundances of both M1/M2 macrophages and CD8 + T cells. Moreover, comparative assessment of the TIME confirmed significantly elevated levels of M1/M2 macrophages and CD8 + T cells in the MS4A1 high-expression group. These results corroborate the subtype classification and underscore the reliability of the subtype classification.

The study by Miner Yang et al. classified OC into three subtypes based on metabolic and immune characteristics: immune-suppressive glycan metabolic subtype (C1), immune-inflammatory amino acid metabolic subtype (C2), and immune-desert endocrine subtype (C3) [46]. In the present work, non-mucinous ovarian cancer with high infiltration of CD20 + B cells exhibited immune characteristics closely resembling those of the C2 subtype, including abundant adaptive immune cell infiltration, such as M1 macrophages and CD8 + T cells, high expression of IFN-γ-related genes, T cell activation, and effective immune responses.

GSLs are potential biomarkers for OC [47] that function as signaling molecules within membrane microdomains (lipid rafts) [48] and play critical roles in cell

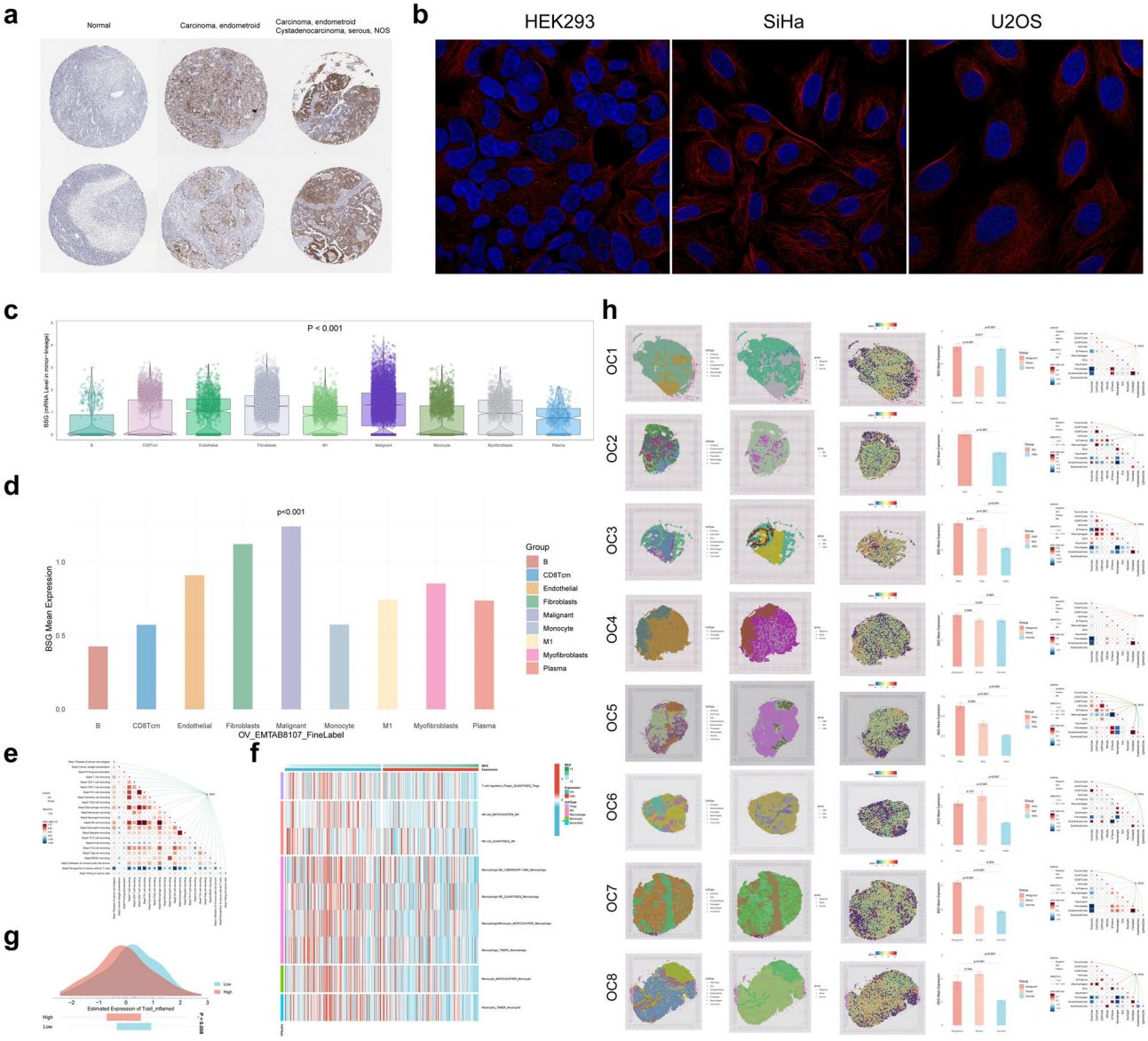

Fig. 6 Multi-dimensional analysis of BSG expression levels in non-mucinous ovarian cancer. (**a**) Immunohistochemical staining results of BSG in "Normal tissue", "Carcinoma, endometroid", and "Carcinoma, endometroid, Cystadenocarcinoma, serous NOS", respectively; (**b**) Immunofluorescence staining results of BSG in HEK293, SiHa, and U2OS cell lines. Green represents the expression of the target gene BSG, red represents microtubules, and blue represents nucleus; (**c**) The distribution of BSG in different cell types and differences in gene expression; (**d**) Expression levels of BSG in various cell types; (**e**) Spearman correlation between the TIP score and gene expression level, as well as autocorrelation between the scores; (**f**) Seven algorithms assesse differences in TIME between the high/low BSG expression groups; (**g**) The cloudrain plot illustrating the differences in inflammatory T cell expression levels between the high and low BSG expression groups; (**h**) Spatial transcriptomics analysis results of eight NOMC tissue sections. The lables of each tissue section are indicated at the left of each row. The first column shows the localization of the identified cells after spatial transcriptomics deconvolution. The second column indicates the spatial localization of different malignant regions. The third column depicts the localizatio n of single-gene spatial transcriptomics. The fourth column compares the expression differences of the BSG gene in high malignant/malignant, low/mixed malignant, and normal regions. The far right column presents a Spearman correlation analysis between gene expression and TIME

migration, adhesion, signal recognition, and differentiation [49]. Immunotherapy targeting GSLs is receiving increasing attention. Antibodies recognizing specific GSLs, designated as stage-specific embryonic antigens (SSEAs), are widely utilized to characterize GSL profiles in embryonic stem cells (ESCs) [50–54]. GD2, a disialoganglioside and member of the glycosphingolipid family, is overexpressed in tumors of neuroectodermal origin. The anti-GD2 monoclonal antibody (MAB) Dinutuximab has been approved for the treatment of high-risk neuroblastoma [55]. GHCer is emerging as a promising non-protein antigen target for cancer immunotherapy. The GHCer tumor vaccine can significantly prolonging the PFS in metastatic breast cancer patients during Phase II

clinical trials [56]. Future applications of novel technologies—such as high-resolution single-molecule imaging and enzyme-mediated activation of radical sources/mass spectrometry (EMARS/MS)—will further elucidate the functions and mechanisms of GSLs in cancer, advancing immunotherapeutic strategies directed at these molecules [48, 57].

The correlation between immune checkpoints and GSL metabolic gene signature suggest that upregulation of GSL metabolism may promote immune checkpoint expression, thereby contributing to tumor immune evasion. Although direct evidence for the regulatory role of GSL metabolism on immune checkpoint expression is currently limited, GSL metabolism has been shown to mediate tumor immune evasion. In a recent study in *Nature*, Soula M et al. proposed that glycosphingolipid synthesis is an essential metabolic pathway for tumor immune evasion. Impairment of GSL synthesis increases IFNGR1 expression on the tumor cell surface, rendering tumors more sensitive to IFN-γ signaling. This allows IFN-γ to more effectively induce growth arrest and pro-inflammatory signaling, thereby enhancing immune-mediated cytotoxicity. In animal models, combining inhibitors of GSL synthesis with PD-1 blockers yielded superior efficacy compared to monotherapy [58]. The efficacy of immune checkpoint blockers in ovarian cancer remains unclear [59]; however, these findings suggest that strategically reprogramming or selectively inhibiting GSL metabolism may be more effective than targeting immune checkpoints alone [60].

In this study, proteomic findings were integrated with single-cell and spatial dimensions through transcriptomic analysis and subsequently leveraged to interpret immune profiling results. The combination of transcriptomics, proteomics, and machine learning enabled the development of a prognostic model, offering clinical insights and demonstrating the power of multi-omics integration in revealing molecular expression patterns and functions. Specifically, proteomic analysis identified elevated SUMF1 expression in non-mucinous ovarian cancer. Subsequent immune profiling revealed that immune response scores—including leukocyte fraction, IFN-γ response, lymphocyte infiltration signature score, and TCR Shannon diversity index—decreased with increasing SUMF1 expression. Further single-cell and spatial transcriptomic analyses demonstrated that SUMF1 expression colocalized with malignant cells and was negatively correlated with immune cells such as B/plasma cells, macrophages, and NK cells.

These findings suggest that tumor cells may upregulate SUMF1 to remodel the TIME, thereby facilitating immune evasion. One potential mechanism involves SUMF1-mediated post-translational modification and activation of sulfatases, which regulate ECM remodeling. Through degradation of glycosaminoglycans such as chondroitin sulfate and other ECM components, SUMF1 alters matrix structure and function [61–63]. The resulting changes in ECM stiffness and architecture can form a physical barrier [64–67], impeding the infiltration of immune cells such as CD8 + T cells and promoting tumor immune evasion [68–71].

To further evaluate the prognostic relevance of the ECM, we employed transcriptomic and proteomic approaches—weighted gene co-expression network analysis (WGCNA) and protein-protein interaction (PPI) analysis—to identify ECM genes co-expressed with SUMF1 and constructed a corresponding prognostic model. These multi-algorithm-based models confirmed the ECM as a key prognostic factor in ovarian cancer and support future combination therapeutic strategies targeting the ECM. We also identified genes with substantial contributions to the prognostic model, providing a basis for subsequent model refinement. Future studies may explore targeting these GSLs or ECM remodeling pathways to develop novel immunotherapies approaches and improve clinical outcomes in ovarian cancer.

Peptidylprolyl isomerase A (PPIA) promotes inflammatory diseases, tumor progression, and tumor resistance [72]. Extracellular PPIA can catalyze the isomerization of its sole known cellular receptor, extracellular matrix metalloproteinase inducer (EMMPRIN, also known as BSG, CD147) [73], which activates downstream signaling pathways and regulating various diseases including inflammatory diseases, coronavirus infections, and cancer [74–76].

Although we were unable to perform experimentals to validate subtype-specific molecular or functional changes due to limitations in funding and time, the expression pattern and functional role of BSG in tumors have been documented in prior studies.

BSG acts as a potent inducer of matrix metalloproteinases (MMPs) and plays a key regulatory role in ECM remodeling. Previous studies have confirmed high BSG expression in ovarian cancer [77, 78]. Our findings further reveal the elevated BSG expression in malignant cells and fibroblasts, with spatial localization at the interface between malignant and normal tissue, consistent with its role in ECM remodeling.

MMPs induced by BSG initiate processes related to ECM degradation, cell adhesion, and cell-cell interactions; BSG also promotes the differentiation of myofibroblasts, which are associated with ECM deposition and contraction [79]. Furthermore, BSG stimulates TGFβ3 expression, thereby upregulating fibronectin and type V collagen [80]. Increased deposition and rearrangement of ECM components such as collagen elevate matrix stiffness, creating a physical barrier that limits the infiltration of T cells and other immune cells into deep tumor

tissues [81]. Moreover, BSG negatively regulates T cell responses through selective inhibition of the Vav1/Rac1 pathway [82] and suppresses T cell-mediated immunity [83]. These mechanisms may explain the negative correlation observed in our study between BSG expression and immune scores, as well as immune cell abundance in the TIME.

The role of BSG in lactate metabolic reprogramming is also well established. Through its specific interaction with monocarboxylate transporter 1 (MCT1), BSG facilitates lactate efflux and prevents intracellular acidosis. This process supports energy metabolism and growth in glycolysis-dependent tumors [84]. In human colon adenocarcinoma cell lines, BSG silencing significantly reduced glycolytic flux and suppressed tumor growth [85]. Furthermore, Zhang et al. used CCK-8, wound healing, Transwell, and flow cytometry assays to show that BSG silencing inhibited tumor cell proliferation, migration, and invasion, disrupted lipid metabolism, and promoted apoptosis [86]. These findings provide important insights into the role of BSG in ovarian cancer immunity, metabolism, and progression.

Despite these novel findings, this study has some limitations. Experiments validation through qPCR, metabolic flux analysis, or immune phenotyping such as CD8 + T cell infiltration would provide deeper insight into the expression pattern and function of BSG in non-mucinous ovarian cancer. However, due to limitations in funding and time, it is not feasible to conduct these experiments within the current study. Our future work will therefore foucus on this to further investigate the subtype-specific molecular or functional alterations. In the spatial transcriptomics analysis, the expression patterns of MS4A1 and SUMF1 across highly malignant, low malignant, and non-malignant tissues were inconsistent across 8 samples. On one hand, this inconsistency may reflect inherent tumor heterogeneity. On the other hand, because the classification of malignant tissues depends on the proportion of malignant cells within each spatial transcriptomics spot, the resolution of these spots and the performance of the markers used to identify malignant cells could also affect the results. The absence of mucinous ovarian carcinoma data in the TCGA public database precluded an investigation of the metabolic and immune characteristics of this subtype. However, since serous ovarian carcinoma represents the most common histological type, the findings retain broad practical significance. Future studies should explore whether these conclusions extend to mucinous ovarian carcinoma and other tumor types.

Conclusions

In conclusion, CD20 + B cells and glycosphingolipid metabolism are key immune and metabolic characteristics of non-mucinous ovarian cancer. The PPIA-BSG-mediated cell communication can facilitate tumor immune evasion through ECM remodeling. Future research should further clarify the interaction between GSL metabolism and TIME, thereby advancing personalized treatment strategies based on immune and metabolic characteristics.

Abbreviations

OC	Ovarian cancer
TIME	Tumor immune microenvironment
HGSOC	High-grade serous ovarian carcinoma
NK cell	Natural killer cell
PD-L1	Programmed death ligand 1
OEC	Ovarian Endometrioid Carcinoma
TILs	Tumor-infiltrating lymphocytes
MSI	Microsatellite instability
Tregs	Regulatory T cells
PGE2	Prostaglandin E2
FAO	Fatty acid oxidation
CCOC	Clear cell ovarian carcinoma
PPP	Pentose phosphate pathway
SOC	Serous ovarian carcinoma
TME	Tumor microenvironment
NAA	N-acetylaspartate
ROS	Reactive oxygen species
NADPH	Nicotinamide adenine dinucleotide phosphate
GWAS	Genome-wide association study
CLSA	Canadian Longitudinal Study on Aging
NMEOC	Non-mucinous epithelial ovarian carcinoma
LGSOC	Low-grade serous epithelial ovarian carcinoma
EEOC	Endometrioid epithelial ovarian carcinoma
EOC	Epithelial ovarian carcinoma
TCGA	The Cancer Genome Atlas
GEO	Gene Expression Omnibus
HPA	Human Protein Atlas
MR	Mendelian randomization
SNPs	Single nucleotide polymorphisms
IVs	Instrumental variables
LD	Linkage disequilibrium
GSVA	Gene set variation analysis
KEGG	Kyoto encyclopedia of genes and genomes
CI	Confidence interval
HR	Hazard ratio
TLS	Tertiary lymphoid structures
TIP	Tracking tumor immunophenotype
UMI	Unique molecular identifier
WGCNA	Weighted gene co-expression network analysis
CV	Coefficient of variation
TOM	Topological overlap measure
GS	Gene significance
MS	Module significance
ROC	Receiver operating characteristic curve
AUC	Area under the curve
GSL	Glycosphingolipid
PFS	Progression-free survival
DSS	Disease-specific survival
OS	Overall survival
MIF	Macrophage migration inhibitory factor
ECM	Extracellular matrix
SSEAs	Stage-specific embryonic antigens
ESCs	Embryonic stem cells
MAB	Monoclonal antibody
EMARS/MS	Enzyme-mediated activation of radical sources/mass spectrometry

SUMF1	Sulfatase modifying factor 1
GEMs	Glycosphingolipid enriched microdomains
ASCT2	Alanine-serine-cysteine transporter 2
UGCG	UDP-glucose ceramide glucosyltransferase
ER	Endoplasmic reticulum
CXCL	CXC ligands
PPIA	Peptidylprolyl isomerase A
EMMPRIN	Extracellular matrix metalloproteinase inducer
MMPs	Matrix metalloproteinases
MCT1	Monocarboxylate transporter 1

Supplementary Information

The online version contains supplementary material available at https://doi.org/10.1186/s13048-025-01877-y.

Supplementary Material 1

Supplementary Material 2

Acknowledgements
Not applicable.

Authors' contributions
HY : Formal analysis, Investigation, Project administration, Methodology, Writing - original draft, Funding acquisition. **CY** : Data curation, Methodology, Supervision, Writing - review & editing. **TX** : Data curation, Visualization, Methodology. **ZZ** : Writing - review & editing. **DW** : Writing - review & editing. **LH** : Writing - review & editing. **LD** : Writing - review & editing. **WZ** :Writing - review & editing. **LW** : Writing - review & editing. **MJ** : Conceptualization. **TZ** : Administration. **YY** : Administration, Conceptualization.

Data availability
The original contributions presented in the study are included in the article, further inquiries can be directed to the corresponding authors.

Declarations

Ethics approval and consent to participate
Not applicable.

Consent for publication
Not applicable.

Competing interests
The authors declare no competing interests.

Received: 27 April 2025 / Accepted: 25 October 2025
Published online: 24 December 2025

References

1. Siegel RL, Giaquinto AN, Jemal A. Cancer statistics, 2024. CA Cancer J Clin. 2024;74:12–49.
2. Veneziani AC, et al. Heterogeneity and treatment landscape of ovarian carcinoma. Nat Rev Clin Oncol. 2023;20:820–42.
3. Matulonis UA, et al. Ovarian cancer. Nat Rev Dis Primers. 2016;2:16061.
4. Yan C, et al. Integrated immunogenomic analysis of single-cell and bulk tissue transcriptome profiling unravels a macrophage activation paradigm associated with immunologically and clinically distinct behaviors in ovarian cancer. J Adv Res. 2023;44:149–60.
5. Wang YK, et al. Genomic consequences of aberrant DNA repair mechanisms stratify ovarian cancer histotypes. Nat Genet. 2017;49:856–65.
6. Mollaoglu G, et al. Ovarian cancer-derived IL-4 promotes immunotherapy resistance. Cell. 2024;187:7492–e75107422.
7. Heinze K, et al. The prognostic effect of immune cell infiltration depends on molecular subtype in endometrioid ovarian carcinomas. Clin Cancer Res. 2023;29:3471–83.
8. Livori K, Calleja-Agius J. Rare but still there: a scoping review on endometriosis-associated ovarian cancer. Discov Med. 2024. https://doi.org/10.24976/Discov.Med.202436182.44.
9. Miao Y, et al. The activation of PPARγ enhances Treg responses through up-regulating CD36/CPT1-mediated fatty acid oxidation and subsequent N-glycan branching of TβRII/IL-2Rα. Cell Commun Signal. 2022;20:48.
10. Magar AG, Morya VK, Kwak MK, Oh JU, Noh KC. A molecular perspective on HIF-1α and angiogenic stimulator networks and their role in solid tumors: an update. Int J Mol Sci. 2024. https://doi.org/10.3390/ijms25063313.
11. Tong Y, Gao WQ, Liu Y. Metabolic heterogeneity in cancer: an overview and therapeutic implications. Biochimica et Biophysica Acta (BBA). 2020;1874:188421.
12. Reinfeld BI, Rathmell WK, Kim TK, Rathmell JC. The therapeutic implications of immunosuppressive tumor aerobic glycolysis. Cell Mol Immunol. 2022;19:46–58.
13. De Rosa V, Di Rella F, Di Giacomo A, Matarese G. Regulatory T cells as suppressors of anti-tumor immunity: role of metabolism. Cytokine Growth Factor Rev. 2017;35:15–25.
14. Yang L, et al. Metabolic shifts toward glutamine regulate tumor growth, invasion and bioenergetics in ovarian cancer. Mol Syst Biol. 2014;10:728.
15. Menga A, et al. N-acetylaspartate release by glutaminolytic ovarian cancer cells sustains protumoral macrophages. EMBO Rep. 2021;22:e51981.
16. Ma G, et al. Reprogramming of glutamine metabolism and its impact on immune response in the tumor microenvironment. Cell Commun Signal. 2022;20:114.
17. Ji JX, et al. The unique metabolome of clear cell ovarian carcinoma. J Pathol. 2024;264:160–73.
18. de Nonneville A, et al. Endometrioid ovarian carcinoma landscape: pathological and molecular characterization. Mol Oncol. 2024;18:2586–600.
19. Nan Y, et al. Otub2 silencing promotes ovarian cancer via mitochondrial metabolic reprogramming and can be synthetically targeted by CA9 inhibition. Proc Natl Acad Sci USA. 2024;121:e2315348121.
20. Orrù V, et al. Complex genetic signatures in immune cells underlie autoimmunity and inform therapy. Nat Genet. 2020;52:1036–45.
21. Chen Y, et al. Genomic atlas of the plasma metabolome prioritizes metabolites implicated in human diseases. Nat Genet. 2023;55:44–53.
22. Li J, Tang M, Gao X, Tian S, Liu W. Mendelian randomization analyses explore the relationship between cathepsins and lung cancer. Commun Biol. 2023;6:1019.
23. Folkersen L, et al. Genomic and drug target evaluation of 90 cardiovascular proteins in 30,931 individuals. Nat Metab. 2020;2:1135–48.
24. Zhao JH, et al. Genetics of circulating inflammatory proteins identifies drivers of immune-mediated disease risk and therapeutic targets. Nat Immunol. 2023;24:1540–51.
25. Ottensmann L, et al. Genome-wide association analysis of plasma lipidome identifies 495 genetic associations. Nat Commun. 2023;14:6934.
26. Dareng EO, et al. Integrative multi-omics analyses to identify the genetic and functional mechanisms underlying ovarian cancer risk regions. Am J Hum Genet. 2024;111(6):1061–83.
27. Kurki MI, et al. FinnGen provides genetic insights from a well-phenotyped isolated population. Nature. 2023;613:508–18.
28. Denisenko E, et al. Spatial transcriptomics reveals discrete tumour microenvironments and autocrine loops within ovarian cancer subclones. Nat Commun. 2024;15:2860.
29. Deng S, et al. ITPRIPL1 binds CD3ε to impede T cell activation and enable tumor immune evasion. Cell. 2024;187:2305–23. e2333.
30. Ravi R, et al. Bifunctional immune checkpoint-targeted antibody-ligand traps that simultaneously disable TGFβ enhance the efficacy of cancer immunotherapy. Nat Commun. 2018;9:741.
31. Wang J, et al. Siglec-15 as an immune suppressor and potential target for normalization cancer immunotherapy. Nat Med. 2019;25:656–66.
32. Yi L, Wu G, Guo L, Zou X, Huang P. Comprehensive analysis of the PD-L1 and immune infiltrates of m6A RNA methylation regulators in head and neck squamous cell carcinoma. Mol Ther Nucleic Acids. 2020;21:299–314.
33. Zeng D, et al. Tumor microenvironment characterization in gastric cancer identifies prognostic and immunotherapeutically relevant gene signatures. Cancer Immunol Res. 2019;7:737–50.
34. Thorsson V, et al. The immune landscape of cancer. Immunity. 2019;51:411–2.

35. Liu Z, et al. Machine learning-based integration develops an immune-derived LncRNA signature for improving outcomes in colorectal cancer. Nat Commun. 2022;13:816.
36. Cheng J, He Z, Jing J, Liu Y, Zhang H. Integrating Machine Learning and Multi-omics to Identify Key SUMOylation Molecular Signature in Sarcoma. *Life Conflux* 1. 2025.
37. Flynn NJ, Somasundaram R, Arnold KM, Sims-Mourtada JJTo. The multifaceted roles of B cells in solid tumors: emerging treatment opportunities. Target Oncol. 2017;12:139–52.
38. Vledder A, et al. B cells critical for outcome in high grade serous ovarian carcinoma. Int J Cancer. 2024;155:2265–76.
39. Berntsson J, Nodin B, Eberhard J, Micke P, Jirström KJI. Prognostic impact of tumour-infiltrating B cells and plasma cells in colorectal cancer. Int J Cancer. 2016;139:1129–39.
40. Thorsson V, et al. The immune landscape of cancer. Immunity. 2018;48:812–30. e814.
41. Chu Y, et al. Pan-cancer T cell atlas links a cellular stress response state to immunotherapy resistance. Nat Med. 2023;29:1550–62.
42. Llovet JM, et al. Immunotherapies for hepatocellular carcinoma. Nat Rev Clin Oncol. 2022;19:151–72.
43. Propper DJ, Balkwill FR. Harnessing cytokines and chemokines for cancer therapy. Nat Rev Clin Oncol. 2022;19:237–53.
44. Xue R, et al. Liver tumour immune microenvironment subtypes and neutrophil heterogeneity. Nature. 2022;612:141–7.
45. Thorsson V, et al. The immune landscape of cancer. Immunity. 2019;51:411–2.
46. Yang M, Chen G, Gao K, Wang YJFO. Tumor immunometabolism characterization in ovarian cancer with prognostic and therapeutic implications . 2021; 11: 622752.
47. Odak Z, et al. Deciphering the interplay: Thieno [2, 3-b] pyridine's impact on glycosphingolipid expression, cytotoxicity, apoptosis, and metabolomics in ovarian. Tumor cell lines. Int J Mol Sci. 2024;25:6954.
48. Furukawa K, et al. New era of research on cancer-associated glycosphingolipids. Cancer Sci. 2019;110:1544–51.
49. Zong W-X, Thompson CBJG, editors. development. (2006) Necrotic death as a cell fate 20: 1–15.
50. Chang W-W, et al. Expression of Globo H and SSEA3 in breast cancer stem cells and the involvement of fucosyl transferases 1 and 2 in Globo H synthesis. Proc Natl Acad Sci U S A. 2008;105:11667–72.
51. Ho M-Y, Yu AL, Yu JJGJ. Glycosphingolipid dynamics in human embryonic stem cell and cancer: their characterization and biomedical implications. Glycoconj J. 2017;34:765–77.
52. Kuo H-H, et al. High expression FUT1 and B3GALT5 is an independent predictor of postoperative recurrence and survival in hepatocellular carcinoma. Scientific Reports. 2017;7:10750.
53. Lou Y-W, et al. Stage-specific embryonic antigen-4 as a potential therapeutic target in glioblastoma multiforme and other cancers. Proc Natl Acad Sci U S A. 2014;111:2482–7.
54. Yu AL, Hung J-T, Ho M-Y, Yu, JJSc. development. Alterations of glycosphingolipids in embryonic stem cell differentiation and development of glycan-targeting cancer immunotherapy. Stem cells and development. 2016;25:1532–48.
55. Yu AL, et al. Anti-GD2 antibody with GM-CSF, interleukin-2, and isotretinoin for neuroblastoma. N Engl J Med. 2010;363:1324–34.
56. Huang C-S, American Society of Clinical Oncology, et al. Randomized phase II/III trial of active immunotherapy with OPT-822/OPT-821 in patients with metastatic breast cancer. J Clin Oncol. 2016. https://doi.org/10.1200/JCO.2016.34.15_suppl.1003.
57. Komura N, et al. Raft-based interactions of gangliosides with a GPI-anchored receptor. Nat Chem Biol. 2016;12:402–10.
58. Soula M, et al. Glycosphingolipid synthesis mediates immune evasion in KRAS-driven cancer. Nature. 2024;633:451–8.
59. Ghisoni E, et al. Immunotherapy for ovarian cancer: towards a tailored immunophenotype-based approach. Nat Rev Clin Oncol. 2024;21:801–17.
60. Chen S, Wang X, Jounaidi Y. UGCG and the glycosphingolipid rheostat: a metabolic checkpoint governing immune activation and tumor immune evasion. Signal Transduct Target Ther. 2025;10:298.
61. Schlotawa L, Adang LA, Radhakrishnan K, Ahrens-Nicklas. RCJljoms. Multiple sulfatase deficiency: a disease comprising mucopolysaccharidosis, sphingolipidosis, and more caused by a defect in posttranslational modification. 2020;21: 3448.
62. Schlotawa L, et al. Drug screening identifies tazarotene and bexarotene as therapeutic agents in multiple sulfatase deficiency. EMBO Mol Med. 2023;15:e14837.
63. Weidner J, et al. Expression, activity and localization of lysosomal sulfatases in chronic obstructive pulmonary disease. Sci Rep. 2019;9:1991.
64. Du W, Xia X, Hu F, Yu JJFI. Extracell Matrix Remodeling Tumor Immun. 2024;14:1340634.
65. Madsen DH, Bugge THJJoCB. The source of matrix-degrading enzymes in human cancer. Probl Res Reproducibility Possible Solutions. 2015;209:195–8.
66. Schedin P, Keely PJJCSHpib. Mammary gland ECM remodeling, stiffness, and mechanosignaling in normal development and tumor progression. 2011; 3: a003228.
67. Cox TR, Erler JT. Molecular pathways: connecting fibrosis and solid tumor metastasis. Clin Cancer Res. 2014;20:3637–43.
68. Juric V, et al. MMP-9 inhibition promotes anti-tumor immunity through disruption of biochemical and physical barriers to T-cell trafficking to tumors. PLoS One. 2018;13:e0207255.
69. Denney H, Clench MR, Woodroofe MNJB, communications br. Cleavage of chemokines CCL2 and CXCL10 by matrix metalloproteinases-2 and-9: implications for chemotaxis. 2009; 382: 341–347.
70. Cox JH, Dean RA, Roberts CR, Overall CM. Matrix metalloproteinase processing of CXCL11/I-TAC results in loss of chemoattractant activity and altered glycosaminoglycan binding. J Biol Chem. 2008;283:19389–99.
71. Van den Steen PE, Husson SJ, Proost P, Van Damme J, Opdenakker G. Carboxyterminal cleavage of the chemokines MIG and IP-10 by gelatinase B and neutrophil collagenase. Biochem Biophys Res Commun. 2003;310:889–96.
72. Yurchenko V, Constant S, Eisenmesser E, Bukrinsky M. Cyclophilin-CD147 interactions: a new target for anti-inflammatory therapeutics. Clin Exp Immunol. 2010;160:305–17.
73. Schlegel J, et al. Solution characterization of the extracellular region of CD147 and its interaction with its enzyme ligand Cyclophilin A. J Mol Biol. 2009;391:518–35.
74. Han JM, Jung HJ. Cyclophilin A/CD147 interaction: a promising target for anticancer therapy. Int J Mol Sci. 2022. https://doi.org/10.3390/ijms23169341.
75. Wang X, et al. Nqo1 triggers neutrophil recruitment and NET formation to drive lung metastasis of invasive breast cancer. Cancer Res. 2024;84:3538–55.
76. Liao EC, et al. PPIA enhances cell growth and metastasis through CD147 in oral cancer. Arch Biochem Biophys. 2025;765:110328.
77. Jin JS, et al. Increasing expression of extracellular matrix metalloprotease inducer in ovary tumors: tissue microarray analysis of immunostaining score with clinicopathological parameters. Int J Gynecol Pathol. 2006;25:140–6.
78. Zhao Y, et al. The role of EMMPRIN expression in ovarian epithelial carcinomas. Cell Cycle. 2013;12:2899–913.
79. Guindolet D, Gabison EE. Role of CD147 (EMMPRIN/basigin) in tissue remodeling. Anat Rec. 2020;303:1584–9.
80. Ohtani H. Stromal reaction in cancer tissue: pathophysiologic significance of the expression of matrix-degrading enzymes in relation to matrix turnover and immune/inflammatory reactions. Pathol Int. 1998;48:1–9.
81. Xiao Z, et al. Nanodrug removes physical barrier to promote T-cell infiltration for enhanced cancer immunotherapy. J Control Release. 2023;356:360–72.
82. Ruiz S, Castro-Castro A, Bustelo XR. CD147 inhibits the nuclear factor of activated T-cells by impairing Vav1 and Rac1 downstream signaling. J Biol Chem. 2008;283:5554–66.
83. Biegler B, Kasinrerk W. Reduction of CD147 surface expression on primary T cells leads to enhanced cell proliferation. Asian Pac J Allergy Immunol. 2012;30:259–67.
84. Walters DK, Arendt BK, Jelinek DF. CD147 regulates the expression of MCT1 and lactate export in multiple myeloma cells. Cell Cycle. 2013;12:3175–83.
85. Le Floch R, et al. CD147 subunit of lactate/H + symporters MCT1 and hypoxia-inducible MCT4 is critical for energetics and growth of glycolytic tumors. Proc Natl Acad Sci USA. 2011;108:16663–8.
86. Zhang N, Liu Z, Lai X, Liu S, Wang Y. Silencing of CD147 inhibits cell proliferation, migration, invasion, lipid metabolism dysregulation and promotes apoptosis in lung adenocarcinoma via blocking the Rap1 signaling pathway. Respir Res. 2023;24:253.

Publisher's Note